Supporting Information

A hydro/oxo-phobic top hole-selective layer for efficient and stable colloidal quantum dot solar cells

Se-Woong Baek,[a,†] Sang-Hoon Lee,[a,†] Jung Hoon Song,[b] Changjo Kim,[a] Ye-Seol Ha,[a] Hyeyoung Shin,[a,d] Hyungjun Kim,[a] Sohee Jeong,[b,c] and Jung-Yong Lee[a,*]

Optical simulations: The charge generation profile and device absorption can be calculated using a transfer matrix formalism (TMF) simulation.[1] For optical simulations, the refractive indices of the organic materials and quantum dots were acquired by spectroscopic ellipsometry (Alpha-SE, J. A. Woollam Co.). The electric field at each position inside the device could be calculated using optical constants and thicknesses of all layers. The number of charge generation, or excited states, was directly related to the energy absorbed in the materials. The number of charge generation could be obtained by calculating the energy absorption at each position using the square of the electric field and the optical constants. *Molecular dynamics* (MD) s*imulations*: MD simulations were performed using the LAMMPS software program.[2] To achieve full equilibration, we performed MD simulations for 10.21 ns by following the procedure from the cohesive energy density (CED) method[3], which combines temperature annealing, volume compression, and NPT ensemble simulations to correctly estimate the equilibrium density and structure of amorphous materials. In the simulation box, we included 27 MeO-TPD molecules, the interatomic potential was described by means of the DREIDING generic force field potential,[4] and quantum mechanical partial charges were used to describe the electrostatics. For the description of O_2 molecules, we used a rigid three-site oxygen model.[5] For the calculation of diffusion constant, we further included 7 O_2 molecules in the simulation cell and performed NVT ensemble simulation for 16 ns at 300 K to calculate the mean squared displacement (MSD). For the calculation of solubility constant (k_H), we separately performed grand canonical ensemble Monte Carlo (GCMC) simulation using Cerius2 program[6] and 10^7 GCMC steps

were used to obtain averaged values at 300 K. To obtain k_H, the O_2 adsorption isotherm calculated from the GCMC simulations was fitted using dual-mode theory[7]: $C = k_H p + C_\infty bp/(1+bp)$, where C is the concentration of the gas, k_H is the Henry's constant, and p is the partial pressure. The last term represents a Langmuir-type isotherm with the saturation concentration of gas (C_∞) and b is the ratio of the rates of adsorption/desorption of the gas molecules.

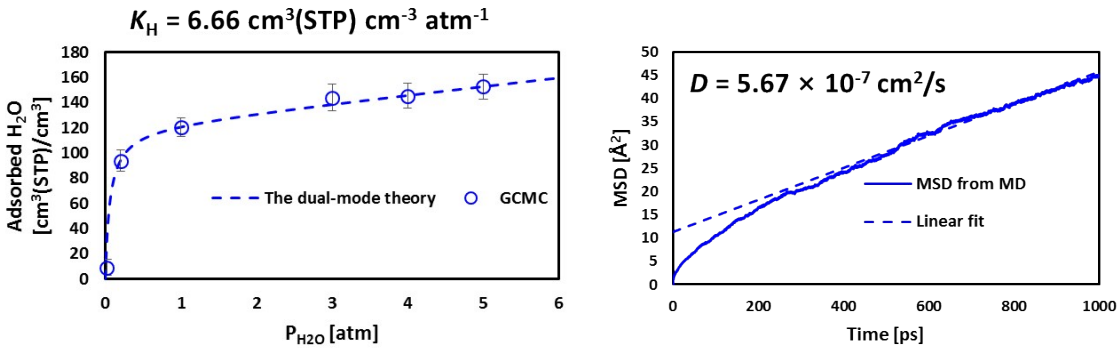

Fig. S1. Transport properties of water in MeO-TPD layer. The water solubility (k_H) and diffusion coefficient (D) of MeO-TPD layer calculated from GCMC and MD simulations, respectively.

The H_2O solubility (k_H) of MeO-TPD was calculated as 6.66 cm^3 (STP) cm^{-3} atm^{-1} similar to the k_H value of polyvinylidiene chloride (PVDC), 6.5 – 10.2 cm^3 (STP) cm^{-3} atm^{-1}, from the previous theoretical study by Coxmuta et al.[8] The diffusion coefficient (D) determined by MSD as a function of simulation time to be 5.67×10^{-7} cm^2 s^{-1}, yielding permeability $P = k_H \times D = 3.78 \times 10^{-6}$ cm^3 (STP) cm^{-1} atm^{-1} s^{-1}. This is comparable to the permeability of 0.5 mm thick polyacrilonitrile (PAN), 2.28×10^{-6} cm^3 (STP) cm^{-1} atm^{-1} s^{-1}, water barrier property as well.

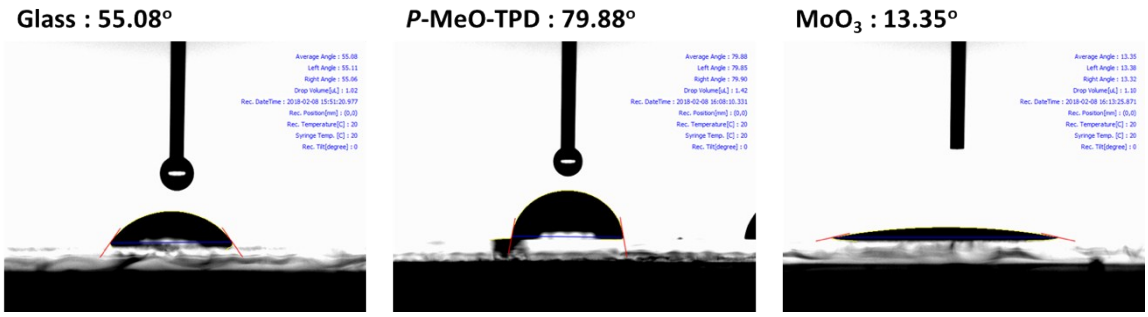

Fig. S2. Hydrophobicity of a *p*-MeO-TPD layer. The contact angle analysis of a *p*-MeO-TPD layer and a MoO_3 layer using DI water as test solution.

Fig. S2 shows a hydrophobic property of a *p*-MeO-TPD layer. To confirm the hydrophobicity of a *p*-MeO-TPD layer, the contact angle analysis was performed using DI water as test solution on glass substrates. The *p*-MeO-TPD layer (79.88°) showed more hydrophobicity compared to the MoO_3 layer (13.35°). Those results support our MD simulation as described in Fig. 1.

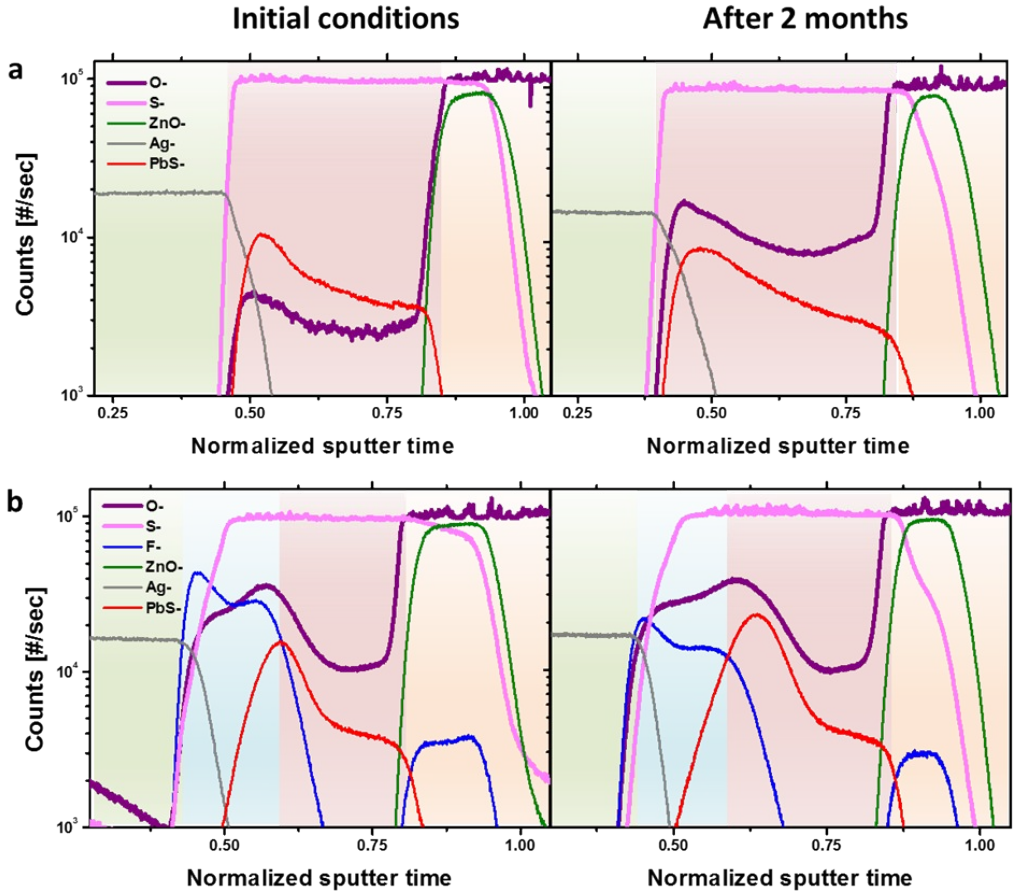

Fig. S3. The time of flight secondary ion mass spectroscopy (TOF-SIMs) of CQDs-based solar cells with and without *p*-MeO-TPD. a, The TOF-SIMs depth profile results of CQDs-based solar cells without HSL before (0 day) (left) and after (60 days) (right) degradation. **b,** The TOF-SIMs depth profile results of CQDs-based solar cell with a *p*-MeO-TPD layer before (0 day) (left) and after (60 days) (right) degradation: (purple) O^-, (pink) S^-, (blue) F^-, (green) ZnO^-, (gray) Ag^-, (red) PbS^-, respectively.

Fig. S3 depicts the TOF-SIMs depth profile results of CQDs-based solar cells with and without a *p*-MeO-TPD layer. The TOF-SIMs results were obtained from full device configurations (ITO/ZnO/PbS/with or without *p*-MeO-TPD/Ag). The anion elements depending on the sputter time clearly confirmed the overall device structure. We detected PbS^- and S^- to finding the PbS region (red area) and F^- to locate the *p*-MeO-TPD layer (blue area). The green and orange areas in Fig. S3 denote

the Ag and ZnO layers, respectively. The element level of the device without HSL clearly showed that the O^- content at the PbS layer (red area, Fig. S3a) significantly increased after 60 days. On the other hand, the O^- content of the device with *p*-MeO-TPD at the PbS layer (red area, Fig. S3b) did not notably change over time.

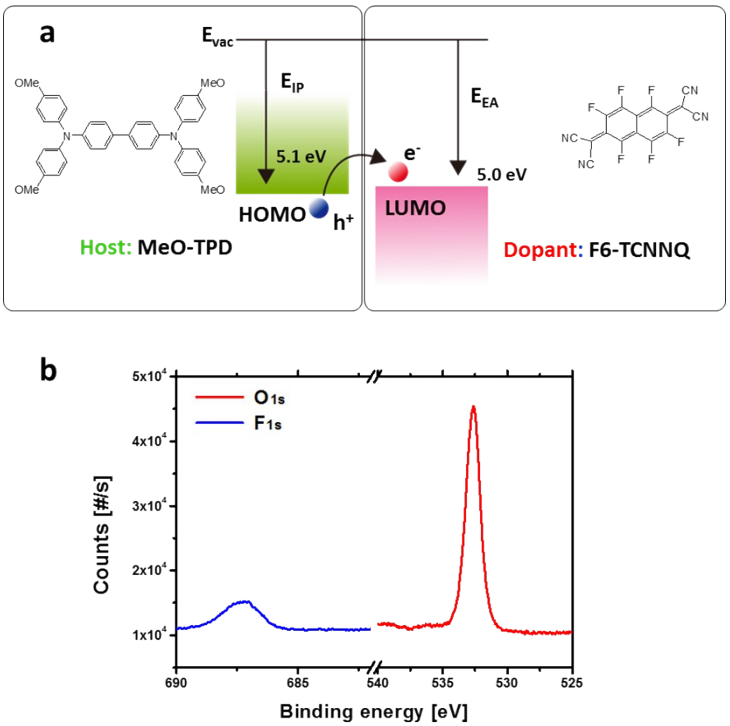

Fig. S4. The doping mechanism and properties of *p*-MeO-TPD layer. a, Schematics of the *p*-type doping mechanism and the molecular structure of MeO-TPD (host material) and F6-TCNNQ (p-type dopant). **b,** The XPS result of a *p*-MeO-TPD layer: O_{1s} (red) and F_{1s} (blue) peaks, respectively.

The energy level of the lowest unoccupied molecular orbital (LUMO) in the F6-TCNNQ dopant allows the transfer of electrons from the highest occupied molecular orbital (HOMO) energy level of the host material (MeO-TPD), generating an excess of free holes in the bulk region, resulting in a highly conductive *p*-doped HSL. Fig. S4 depicts the XPS results of *p*-MeO-TPD layer to confirm the doping concentration. The F_{1s} could be detected only in F6-TCNNQ dopant and O_{1s} could be detected

only from MeO-TPD host; therefore, the doping concentration could be determined by O/F atomic ratio. We calculated the *p*-doping concentration of *p*-MeO-TPD layer as approximately 8.4 wt%.

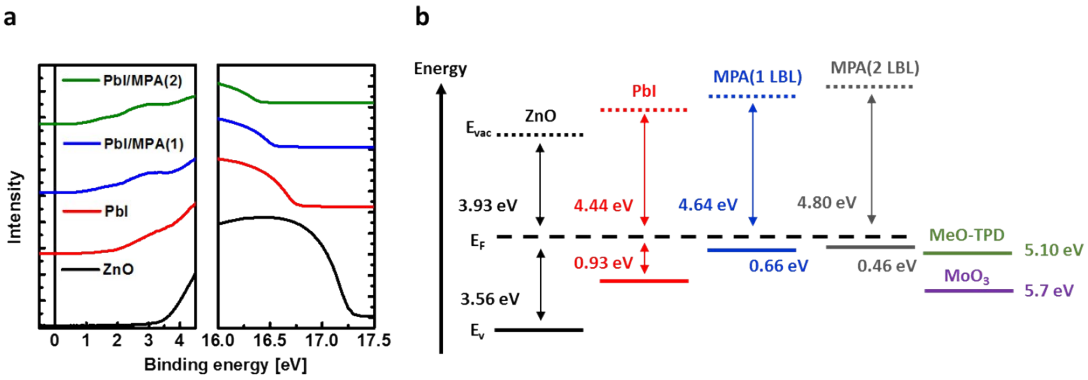

Fig. S5. The ultraviolet photoelectron spectroscopy (UPS) and band energy levels of PbS layers. a, The binding energy spectra: ZnO layer (black), ZnO/PbS-PbI layer (red), ZnO/PbS-PbI/PbS-MPA(1 LBL) layer (blue), and ZnO/PbS-PbI/PbS-MPA(2 LBL) layer (green), respectively, **b,** The energy level diagram estimated from the results of Fig. S5a.

Fig. S54 shows UPS results and the energy level diagram for PbS QDs layers and two hole selective layers (HSLs) (i.e. MeO-TPD and MoO_3). The samples were prepared with the same fabrication conditions. A PbS-PbI layer showed large E_v-E_f (0.93 eV). As the number of PbS-MPA layer increased, the E_v-E_f was gradually reduced, turning to the *p*-type. The final valence band of PbS layer was 5.26 eV, which is well aligned with a *p*-MeO-TPD layer (5.1 eV).

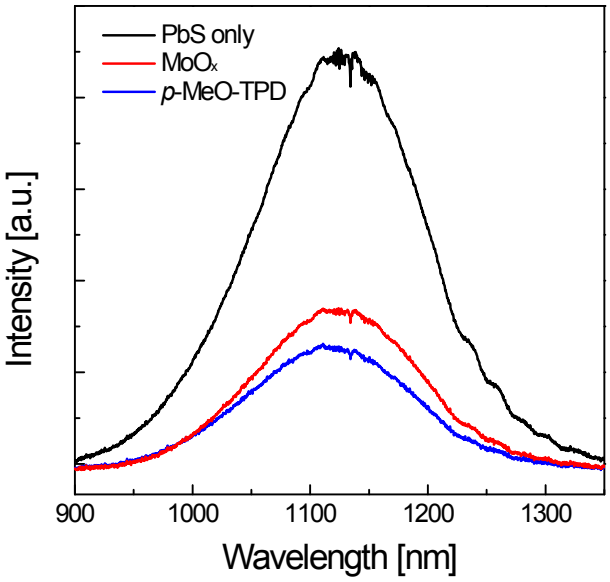

Fig. S6. The PL intensity of CQDs layers without (black) and with a MoO_x (red) and a *p*-MeO-TPD (blue) layer.

Fig. S6 depicts the PL measurement results of CQDs with HSL layers. For the PL measurement, both *p*-MeO-TPD and MoO_x layers were deposited on the CQDs (300 nm) / glass substrates. PL spectrums were acquired using LabRAM HR Evolution Visible-NIR model from HORIBA. A 633 nm laser was used as an excitation source. The *p*-MeO-TPD film decreased the PL intensity further, implying more efficient charge extraction of *p*-MeO-TPD compared to MoO_x.

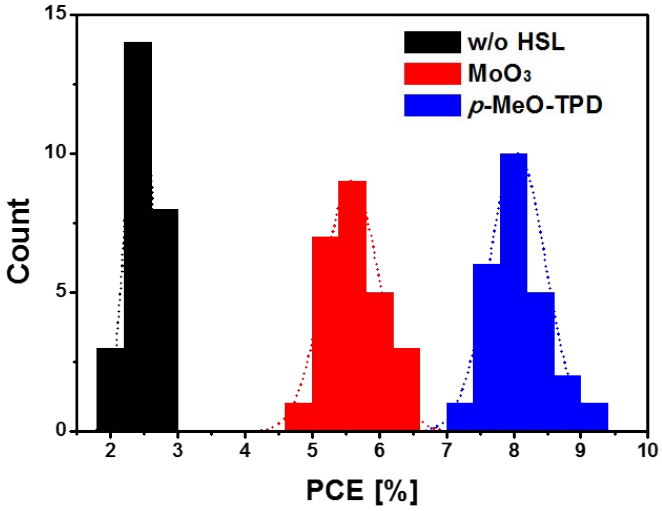

Fig. S7. The statistical histogram of devices performance without and with HSL (MoO_3, *p*-MeO-TPD). The statistical histogram for the device performance based on the 25 devices (black) without HSL, (red) with MoO_3 layer, and (blue) with *p*-MeO-TPD layer, respectively.

Fig. S7 depicts the statistical histogram for the power conversion efficiency (PCE) based on the 25 devices. The *p*-MeO-TPD-deposited device clearly showed improved performance compared to the MoO_3-deposited devices. All devices were fabricated using the same PbS CQDs batch and size.

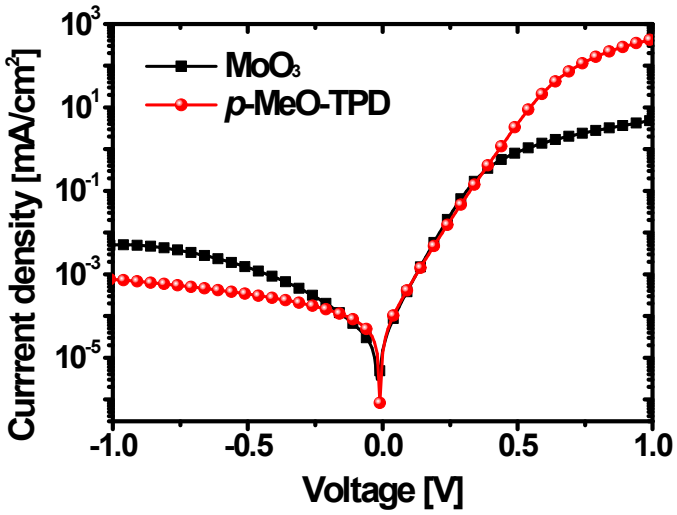

Fig. S8. *J-V* characteristics of solar cells with deposited MoO_3 (black squares) and *p*-MeO-TPD (red circles) layers under dark conditions.

We used a double diode model to obtain the series resistances from the *J-V* curves under a dark condition as shown in Fig. S8. The *J-V* curves are fitted according to the equations, [$I = (R_p/(R_s+R_p))(I_s(\exp(q(V-IR_s)/nkBT)-1)+V/R_p)-I_{ph}$] from previous studies.[9] The best fit gave a series resistance of 1.97 Ω cm^2 for a *p*-MeO-TPD device and 365 Ω cm^2 for a MoO_3 device. Detail fitting parameters were $J_s = 1.62 \times 10^{-15}$ mA/cm^2, n = 1.64, R_s= 1.97 Ω·cm^2, R_p = 3749 kΩ·cm^2 for a *p*-MeO-TPD device, and $J_s = 6.57 \times 10^{-6}$ mA/cm^2, n = 1.26, R_s= 365 Ω cm^2, R_p = 1995 kΩ·cm^2 for a MoO_3 device.

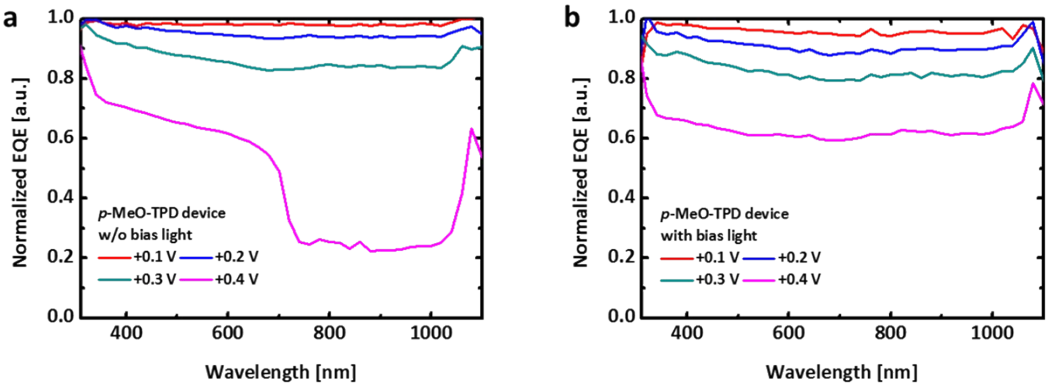

Fig. S9. The normalized EQE of a *p*-MeO-TPD-deposited device at various forward bias conditions. The normalized EQE results measured under a dark condition **a,** and under a bias light condition **b**.

The wavelength dependent EQE reduction of *p*-MeO-TPD-deposited device under a forward bias was observed in such conditions as high forward bias voltage and without bias light illumination during EQE measurements. Current values from the EQE light source are similar to dark current values of the devices. Therefore, wavelength dependent EQE reduction was clearly observed under a forward bias condition. As explained in the manuscript, the wavelength dependent EQE reduction occurred due to highly injected holes from the *p*-MeO-TPD layer. These high injection of holes under a forward bias condition creates a charge accumulation region near the HSL and generated charges near the *p*-MeO-TPD layer in the longer wavelength (700 ~ 1000 nm) easily recombine with those injected charges, resulting in the wavelength dependent EQE reduction. On the other hand, both under a low forward bias voltage and bias light conditions, the injected charge accumulation disappeared due to the low carrier injection and the bias light currents, respectively. As a result, the wavelength dependent EQE reduction was not clearly observed under the low forward bias voltage and the light bias condition as shown in Fig. S9.

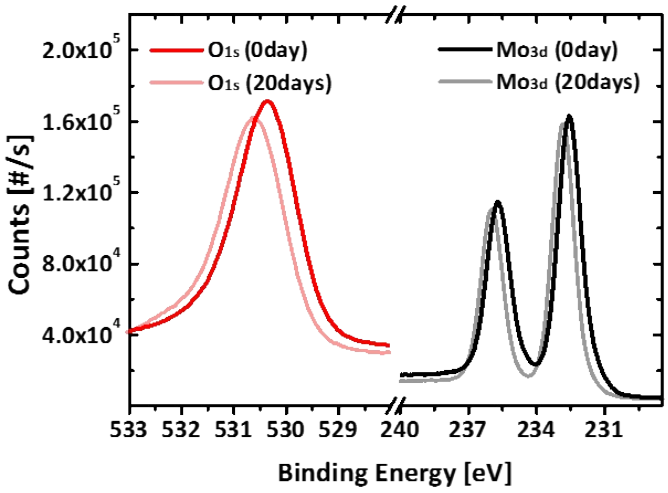

Fig. S10. The XPS result of a MoO_3 layer for stability assessment. The XPS results of MoO_3 layer corresponding to Mo_{3d} (black) and O_{1s} (red) peaks before (dark) and after (bright) degradation, respectively.

Fig. S10 depicts the XPS results of a MoO_3 layer to observe the stoichiometry change of O/Mo ratio. Air exposure of the MoO_3 layer leads to change the binding energy of their components. The binding energy spectra of O_{1s} and Mo_{3d} were shifted to the higher binding energy. These data clearly showed the change of O/Mo ratio increased from 2.7 to 3.2, implying the increased oxygen contents after air exposure. It can be implied the reduction of conductivity originated from the variance of oxidation state in the MoO_3 layer.

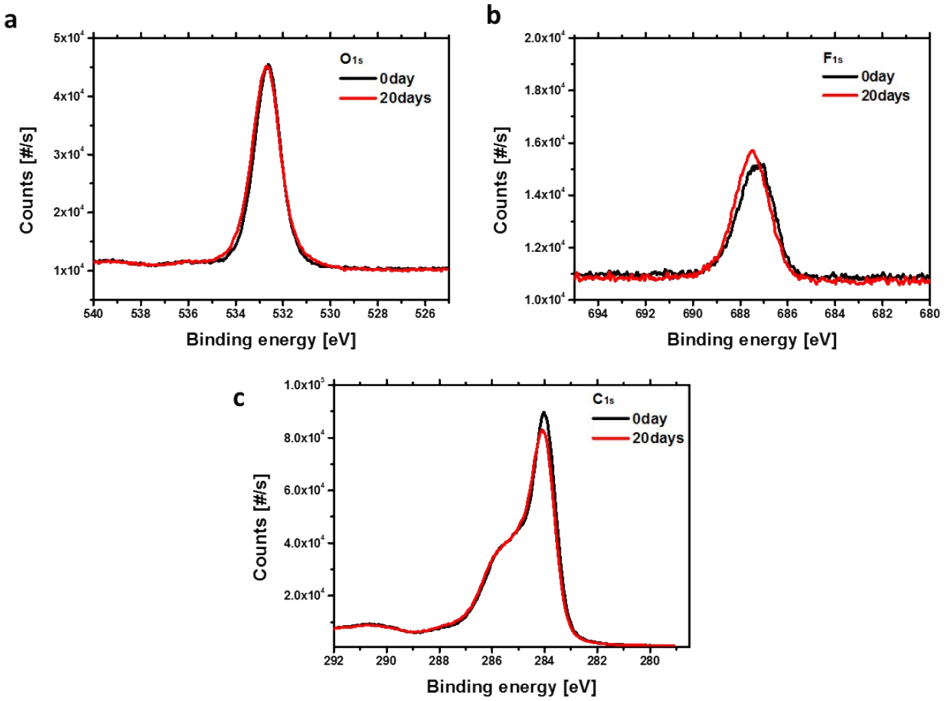

Fig. S11. The XPS results of *p*-MeO-TPD layer for stability assessment. The XPS result of *p*-MeO-TPD layer each corresponding to **a,** $O_{1s,}$ **b,** F_{1s} and **c,** C_{1s} peaks before (0 day) (black) and after (20 days) (red) degradation, respectively.

Fig. S11 depicts the XPS results of a *p*-MeO-TPD layer to carefully study the stability performance. Compared to the MoO_3 layer, O_{1s} peak was not notably changed after 20 days. In addition, doping concentration also showed marginal change. These results suggest that the *p*-MeO-TPD layer is relatively stable compared to the MoO_3 layer.

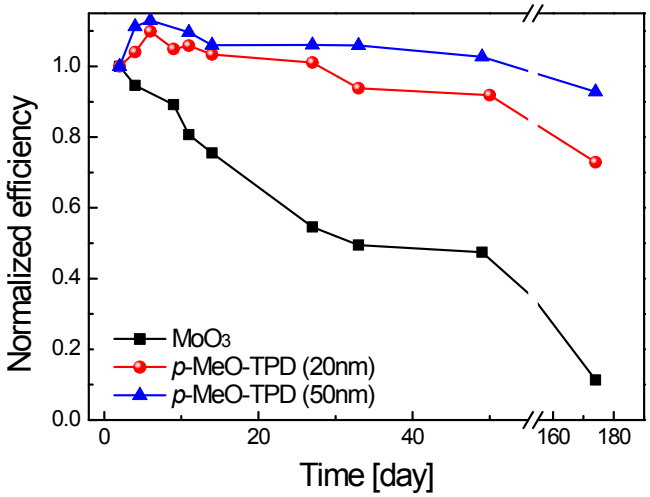

Fig. S12. The stability performance of HSL-deposited CQDs device. The normalized efficiency of MoO_3 (black) and *p*-MeO-TPD layer depending on the thickness; 20 nm (red) and 50 nm (blue)

Fig. S12 depicts the stability performance of CQDs devices depending on the *p*-MeO-TPD layer thickness. The *p*-MeO-TPD layer devices always showed higher stability performance than the MoO_3 device. In addition, even higher stability was achieved with a thicker *p*-MeO-TPD, suggesting that the blocking effect of the *p*-MeO-TPD layer boosted the CQDs device stability.

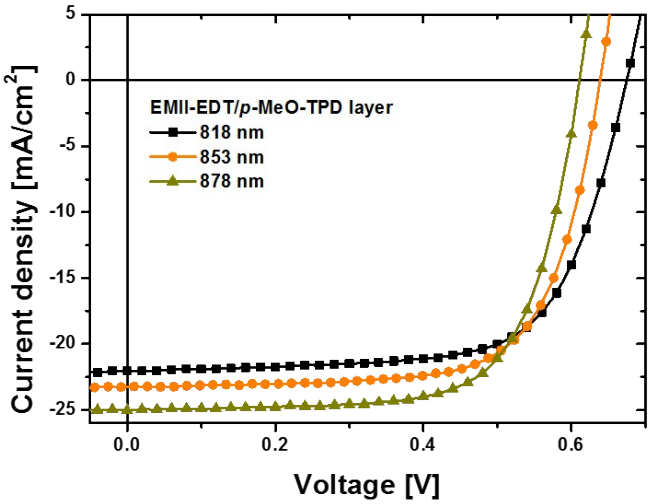

Fig. S13. The *J-V* characteristics of EMII-based CQDs device using various sizes of PbS QDs. The *J-V* curves of *p*-MeO-TPD deposited CQDs devices at various first excitonic peaks of PbS QDs: (black) 818 nm, (bright yellow) 853 nm and (dark yellow) 878 nm, respectively.

Fig. S13 shows the *J-V* characteristics of EMII-based device with a *p*-MeO-TPD layer using various sizes of PbS QDs. We tested three PbS QDs batches such that first excitonic peaks are 818 nm, 853 nm, and 878 nm. The detailed photovoltaic characteristics are described in Table S1. As shown in Fig. S13 and Table S1, The V_{oc} was reduced and J_{sc} was improved as the size of PbS QDs became larger. The highest PCE of 10.7 % was achieved with 878 nm.

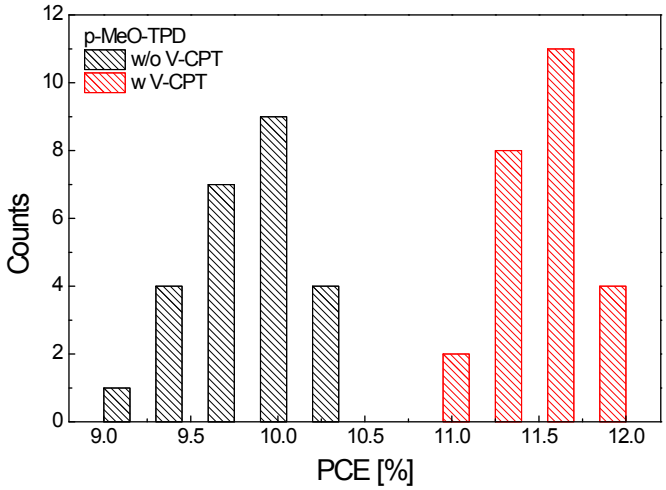

Fig. S14. The statistical histogram of device performance. The histogram of *p*-Meo-TPD-deposited devices without (black) and with (red) V-CPT light trapping schemes. We characterized 25 devices at each condition.

Fig. S14 depicts statistical PCE histograms of 25 devices. A 818 nm PbS CQDs was used for *p*-MeO-TPD-deposited devices and those devices performance were characterized with and without V-CPT. The results clearly showed that the V-CPT light trapping schemes improved the PCE of *p*-MeO-TPD-deposited devices significantly.

Table S1. Photovoltaic characteristics of EMII-based device depositing *p*-MeO-TPD with various sizes of PbS QDs.

1st excitonic peak	V_{oc} [V]	J_{sc} [mA/cm^2]	*FF* [%]	η [%]
818 nm	0.675	22.02	68.31	10.15
853 nm	0.647	23.25	69.72	10.49
878 nm	0.611	25.03	69.84	10.68

References

1. L. A. Pettersson, L. S. Roman and O. Inganäs, *J Appl Phys*, 1999, **86**, 487-496.
2. M. Belmares, M. Blanco, W. A. Goddard, 3rd, R. B. Ross, G. Caldwell, S. H. Chou, J. Pham, P. M. Olofson and C. Thomas, *J Comput Chem*, 2004, **25**, 1814-1826.
3. S. Plimpton, *J Comput Phys*, 1995, **117**, 1-19.
4. S. L. Mayo, B. D. Olafson and W. A. Goddard, *J Phys Chem-Us*, 1990, **94**, 8897-8909.
5. L. Zhang and J. I. Siepmann, *Theor Chem Acc*, 2006, **115**, 391-397.
6. Cerius2 v 4.10, Accelrys, San Diego, CA, (2005).
7. V. T. Stannett, W. J. Koros, D. R. Paul, H. K. Lonsdale and R. W. Baker, in *Chemistry*, Springer Berlin Heidelberg, Berlin, Heidelberg, 1979, DOI: 10.1007/3-540-09442-3_5, pp. 69-121.
8. I. Cozmuta, M. Blanco and W. A. Goddard, 3rd, *J Phys Chem B*, 2007, **111**, 3151-3166.
9. B. P. Rand, D. P. Burk and S. R. Forrest, *Physical Review B*, 2007, **75**, 115327.